

Numerical Simulation of a Variable-Density Mixing-Layer

J. Reinaud L. Joly P. Chassaing
ENSICA 1, Place Emile Blouin Toulouse, France
reinaud@ensica.fr, laurent@ensica.fr, chassaing@ensica.fr

Abstract

The development of a baroclinic secondary instability over the primary Kelvin-Helmholtz roll-up of a two-dimensional, variable-density mixing-layer is discussed. A particular attention is paid to the accuracy of the simulations by investigating the conservation of an invariant of the flow. Then, the influence of both the spatial and the temporal resolution on the development of the secondary instability is studied. It is concluded that the variable-density layer exhibits a strongly unstable region where vorticity has been intensified by the local acceleration coupled with the density stratification.

1 Introduction

Within the context of variable-density shear flows, the generation-destruction of vorticity by the baroclinic torque may alter the dynamics of the flow [1,2]. The focus of the present paper is on the baroclinic secondary instability of a two-dimensional incompressible mixing layer. Such a situation is generic of more complex flows occurring in high Reynolds number binary mixing of fluids of different densities or in thermal mixing. The baroclinic torque is due to the misalignment between the pressure gradient and the density gradient. As seen from the momentum equation the pressure gradient itself may result either from inertial effects [3,4,5], external forcing - as in the case of buoyancy-driven flows under the Boussinesq approximation [2,6] - or a combination of the two effects [7]. The focus is on high Reynolds number variable density flows that are definitely in the inertial regime and well beyond the Boussinesq approximation.

The Blob Vortex Method has been extended to handle the transport a scalar such as in a temporally growing two-dimensional shear layer [8]. In the “transport element method”, applied to variable density flows, both the vorticity and the local scalar gradient are attached to the elements. We propose to revisit the accuracy issue of this method which bases have been set in the pioneering work of Ghoniem *et al.* [6,5]. The section II. is devoted to a simple illustration of the baroclinic generation of vorticity. The formulation of the scheme is derived in section III and a special paragraph compares alternative versions of the numerical procedure. The simulation of a temporally growing unbounded forced shear layer is described in section IV. The simulation reveals a baroclinic secondary instability due to the intensification and straining of the vorticity sheets. These secondary structures are shown to come out from an accurate but fragile resolution. The ability of the method to capture small-scale motions associated with intense baroclinic generation of vorticity is established. It is also concluded that the observed secondary structures arise even when the subharmonic pairing mode is excited.

2 The baroclinic generation of vorticity

The evolution of an incompressible, inviscid, variable-density, zero Richardson number, unbounded two-dimensional flow is investigated. The flow is governed by the variable-density Euler equations

$$\frac{d\rho}{dt} = 0 \quad \nabla \cdot \mathbf{u} = 0 \tag{1a}$$

$$\rho \frac{d\mathbf{u}}{dt} = -\nabla p \tag{1b}$$

Taking the curl of the momentum equation (1b) yields the transport equation of the vorticity

$$\frac{d\boldsymbol{\omega}}{dt} = \nabla p \times \nabla \left(\frac{1}{\rho} \right) \tag{2}$$

Hence the vorticity budget exhibits a source term : the baroclinic torque. As quoted by Turner [9], this is the main difference that distinguishes uniform density flows and non-homogeneous flows.

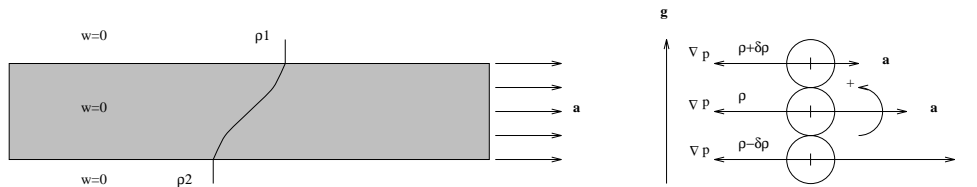


Figure 1: Geometry of the flow and interpretation of vorticity production

An elementary vorticity production by the baroclinic torque is presented. The test flow, described on figure 1, is a stratified, initially irrotationnal fluid domain, submitted to an uniform acceleration in the x -direction at $t = 0$. The initial stratification of density is Gaussian and characterized by its standard deviation σ . The problem is normalized by the spanwise length scale σ , the acceleration a_0 . The density ratio is $\rho_1/\rho_2 = 3.0$.

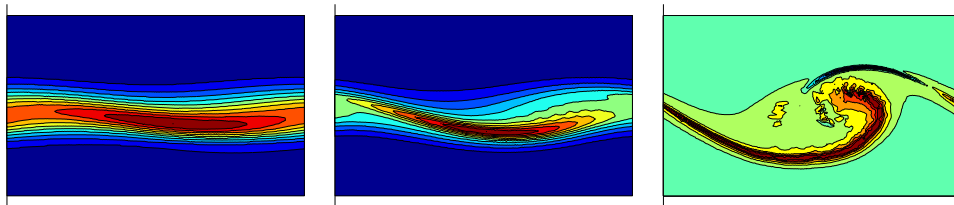


Figure 2: Iso-vorticity lines for the stratified, accelerated layer at $t = 5$, $t = 7.0$ and $t = 9.0$

The vorticity production by the baroclinic torque can easily be interpreted. As shown on figure 1, the layer is uniformly accelerated. Without perturbation, the flow remains parallel so that the pressure is uniform in the y -direction. Then, the acceleration, as well as velocity, is higher where

the density is low, which leads a vorticity layer on the density-gradient layer. This exemple gives a simple illustration of vorticity generation due to pure inertial effects.

When the flow is tilded by a sinewave, with $\lambda = 13.2$ the most unstable wavelength of the mixing layer [10], a roll-up develops as in a standard mixing layer, see figure 2.

3 The Formulation and Numerical Scheme

The numerical scheme aims at tracking a collection of elements carrying both the local vorticity and the density gradient distributed over a circular core characterized by its radius δ . This distribution is needed to desingularize the problem and to reach higher orders of accuracy [11,12].

The equations are then:

$$\frac{d\mathbf{x}}{dt} = \mathbf{u}(\mathbf{x}, t) \quad (3)$$

$$\frac{d\boldsymbol{\omega}}{dt} = \frac{d\mathbf{u}}{dt} \times \frac{\nabla\rho}{\rho} \quad (4)$$

$$\frac{d\mathbf{g}}{dt} = -{}^t[\nabla\mathbf{u}] \cdot \mathbf{g} \quad (5)$$

The velocity field can thus be obtained via the discrete, regularized Biot-Savart law [13,14] while the density is similarly deduced from a summation over its own gradient field [6]:

$$\mathbf{u}(\mathbf{x}, t) = \int \int \mathbf{K}_\delta(\mathbf{x} - \mathbf{x}') \boldsymbol{\omega}(\mathbf{x}', t) d\mathbf{x}' \quad \rho(\mathbf{x}, t) = \int \int \mathbf{L}_\delta(\mathbf{x} - \mathbf{x}') \cdot \mathbf{g}(\mathbf{x}', t) d\mathbf{x}' + \rho_p \quad (6)$$

$$\mathbf{K}(\mathbf{x})_\delta = \frac{1}{2\pi|\mathbf{x}|^2} \begin{pmatrix} -y \\ x \end{pmatrix} * f_\delta, \quad \mathbf{L}(\mathbf{x})_\delta = \frac{1}{2\pi|\mathbf{x}|^2} \begin{pmatrix} x \\ y \end{pmatrix} * f_\delta \quad (7)$$

f_δ is the cut-off function and ρ_p is the potential component depending on boundary conditions. In the calculations, the regularized kernels (K4) are deduced from the Gaussian functions [12]:

$$f_\delta(r) = \frac{1}{\pi\delta^2} \left(2e^{-\frac{r^2}{\delta^2}} - \frac{1}{2}e^{-\frac{r^2}{2\delta^2}} \right) \quad (8)$$

that lead to a fourth-order accuracy as far as the overlapping between neighboring elements is maintained [15]. A standard second-order cut-off function from the same family [12] is also used for reference and the associated kernels will be referred to as K2.

An alternative form of equation (5), providing significant computational savings, is available from [3,4]. This equation is obtained by combining the equation governing the local stretching of a material line with the transport equation of the density gradient (5) :

$$\frac{|\mathbf{g}|}{|d\boldsymbol{\ell}|} = cst \quad \mathbf{g} \cdot d\boldsymbol{\ell} = 0 \quad (9)$$

As far as the discrete description of the stretching is concerned, $|d\ell|$ is replaced in (9) by Δl which measures the spatial separation between neighboring elements. Among possible solutions the following centered scheme, referred to as G2, is proposed :

$$\Delta l_i = \frac{1}{2} (|\mathbf{x}_{i+1} - \mathbf{x}_i| + |\mathbf{x}_i - \mathbf{x}_{i-1}|) \quad (10)$$

which is in contrast with the previously proposed scheme [5] referred to as G1 :

$$\Delta l_i = \frac{1}{2} |\mathbf{x}_{i+1} - \mathbf{x}_{i-1}| \quad (11)$$

The difference stands in the sensitivity of G2 to the curvature of isopycnic lines. The G1 scheme underestimates the deformation when dealing with folding mechanisms that eventually produce curvature radii close to the separation h . The direction of the density gradient is approximated by taking the normal to the tangent of the isopycnic line \mathbf{t} :

$$\mathbf{t}_i = \frac{\mathbf{x}_{i+1} - \mathbf{x}_{i-1}}{|\mathbf{x}_{i+1} - \mathbf{x}_{i-1}|} \quad (12)$$

The acceleration of the elements is obtained via finite backward difference schemes.

The accuracy of the vortex blob method depends also on the overlapping $-\delta > h$ between neighboring vorticity elements [15]. But as the local straining field tends in some places to coarsen the curvilinear mesh of the isopycnic line it may lead to an important growth of errors. The solution proposed in [8,3,5,7] is a continuous refinement (or relaxation) of the curvilinear mesh that inserts (or removes) elements. While local area and circulation are conserved, the distance between two neighboring vortices is kept in the following range :

$$0.5 h \leq |\mathbf{x}_i - \mathbf{x}_{i+1}| \leq 1.5 h \quad (13)$$

This insertion and removal procedure is effective along the isopycnic lines only. This is not fully satisfactory since the spacing between vortices in the direction normal to the isopycnic line is subjected to excursions beyond the limits stated by (13). Though it has been put forth by [8] that the main strain is essentially parallel to isopycnic lines, the reason why the perpendicular direction is not tested stands in the necessity to attach each vortex element to a particular isopycnic line in order to solve equation (9), together with the need to refine the discretisation of those lines.

Dealing with periodic flows, the contribution of all the elements outside of the computational domain must be taken in account. As the Gaussian functions are rapidly decreasing, the associated contribution of all the images of an element in the kernels is only computed over the studied period and the two neighboring ones. The other contribution decreasing with $1/r$ where r is the distance between two vortices is analytically calculated [7,8].

The different versions of the numerical tool are presented. The differences stand in the order of the temporal integration of the location of the elements and their vorticity (second or fourth order Runge-Kutta scheme), the way they are updated (simultaneously or in two fractional steps), the order of the cut-off function, the choice of the scheme to measure the local stretching and finally the order of the finite difference scheme for the acceleration.

ref.	\mathbf{x}	$\boldsymbol{\omega}$	K_δ	$\nabla\rho$	$\frac{d\mathbf{u}}{dt}$	Cost per iteration
RK2S	RK2	RK2	K2	G1	$O(2)$	1
RK2Sb	RK2	RK2	K4	G1	$O(2)$	1
RK4F	RK4	Fractional	K4	G1	$O(1)$	1.8
RK4S	RK4	RK4	K4	G2	$O(2)$	2

Table 1: Description of the numerical tools and their relative computational cost per iteration

4 The temporal mixing layer

4.1 Background

The effect of a non-uniform density field over a shear layer has been already studied for a temporal layer [5] and for a spatially developing layer [3,4]. The main features that come out of those contributions are twofold:

- i)* The relative primary eddy convective speed ($U_c - (U_1 + U_2)/2$) has the sign of the relative velocity of the heavy flow. Vortex simulations showed a good agreement between the calculated convective speed and the empirical formula proposed by Dimotakis [16].
- ii)* The center of the eddy is displaced toward the light flow. The explanation is detailed in [3,4,5]. The baroclinic torque produces vorticity with the same sign of the initial vorticity layer toward the low-density flow and opposite vorticity toward the high-density flow. In this context one can imagine that a dipole is superimposed to a reference, uniform-density case. This dipole induces the displacement of the structure and a non-symmetric entrainment: more light fluid is entrained.

Other interpretations have also been obtained considering pressure forces [16].

4.2 Geometry and initial conditions

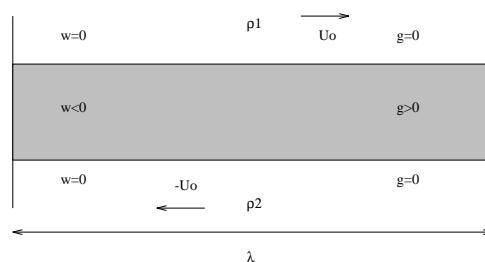


Figure 3: Geometry of the temporal shear layer

The geometry of the flow is given on figure 3. The temporal layer is a mathematical idealization of a physical spatially developing layer obtained by the transformation $x = U_m * t$ where U_m is the mean velocity. It has been shown that the model is not able to capture the natural dissymmetry of the flow due to inertial effects (even in the uniform-density case) because of the periodicity

conditions imposed [17,18,4]. But this model, which reduces the computational domain allows to go further in the description of the small scales motions.

The initial vorticity distribution is Gaussian [8]:

$$w(x, y) = -\frac{\Delta U}{\sqrt{\pi}\sigma} e^{-\frac{y^2}{\sigma^2}} \tag{14}$$

which leads to an error function velocity profile. This model is supported by experimental evidences [19] as well as an initial density gradient field defined [3] by

$$\nabla\rho(x, y) = \begin{pmatrix} 0 \\ \frac{\rho_1 - \rho_2}{\sqrt{\pi}\sigma} e^{-\frac{y^2}{\sigma^2}} \end{pmatrix} \tag{15}$$

The problem is scaled by the vorticity layer thickness σ , the mean speed $U_0 = \Delta U/2$ and the density ρ_2 . The density ratio is $\rho_1/\rho_2 = 3.0$. In these calculations, the temporal layer is perturbed by a monochromatic sinewave. The wavelength corresponds to the box length. It has been taken as the most unstable wavelength of the uniform-density case, $\lambda = 13.2\sigma$ [5]. The amplitude of the perturbation is taken as 1% of λ . Then we compare different calculations.

4.3 Efficiency tests for the mixing layer calculations

It can easily be shown that the circulation over a period remains theoretically constant and that $\Gamma = -2\lambda U_0$. We investigate the ability of the computation to conserve the circulation, comparing several numerical schemes. The numerical parameters are : the initial distance between two neighboring vortices is $h = 0.3$ and the cut-off parameter is $\delta = 0.375$. So as to compare the

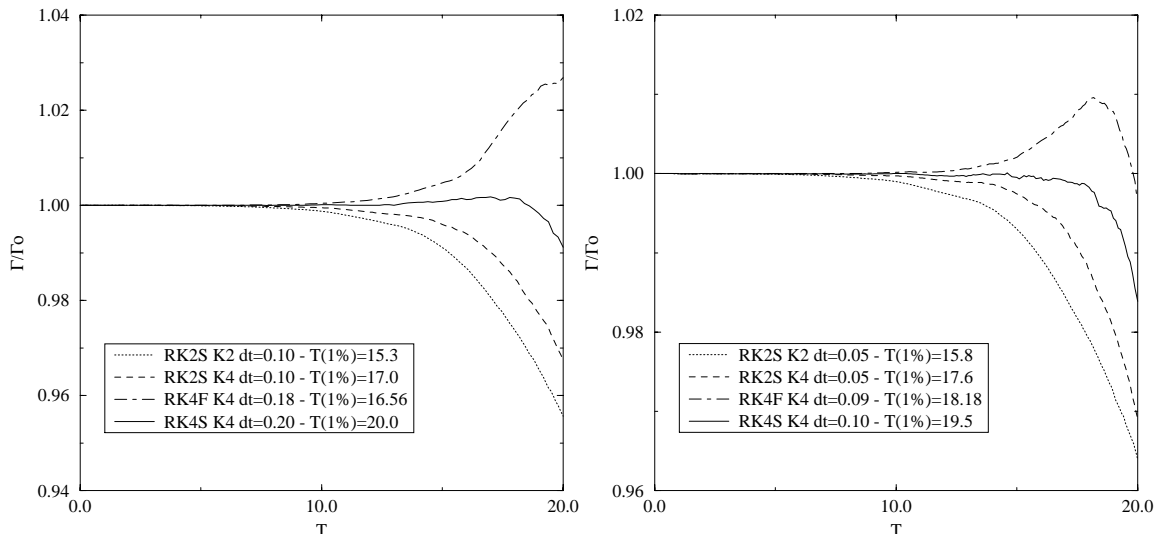


Figure 4: Temporal evolution of the reduced circulation over a period

different versions of the numerical tool, the time steps have been chosen so that the computational cost is the same in the four cases. Figures 4 show two sets of tests. Considering any of those two sets, the RK4S version occurs to be the more accurate as it allows longer integration time

while keeping the relative error on the circulation under 1%. Besides, none of the three alternative versions (RK2S K2 $dt=0.05$, RK2S K4 $dt=0.05$, RK4F K4 $dt=0.09$) has reached the accuracy of RK4S K4 $dt=0.2$ even if their computational cost is twice. It is so demonstrated that high order schemes are more efficient. They allow to go further in time with a lower computational cost. In all the following studies, the RK4S version is used.

4.4 The secondary instability of a variable-density mixing layer

The occurrence of the secondary instability is analyzed first. The computational parameters of this rather resolved simulation are $h = 0.05$, $\delta = 0.0625$, $dt = 0.1$. The initial mesh handles 73 isopycnic lines discretized by 264 elements. The figure 5 shows the vortex element positions during

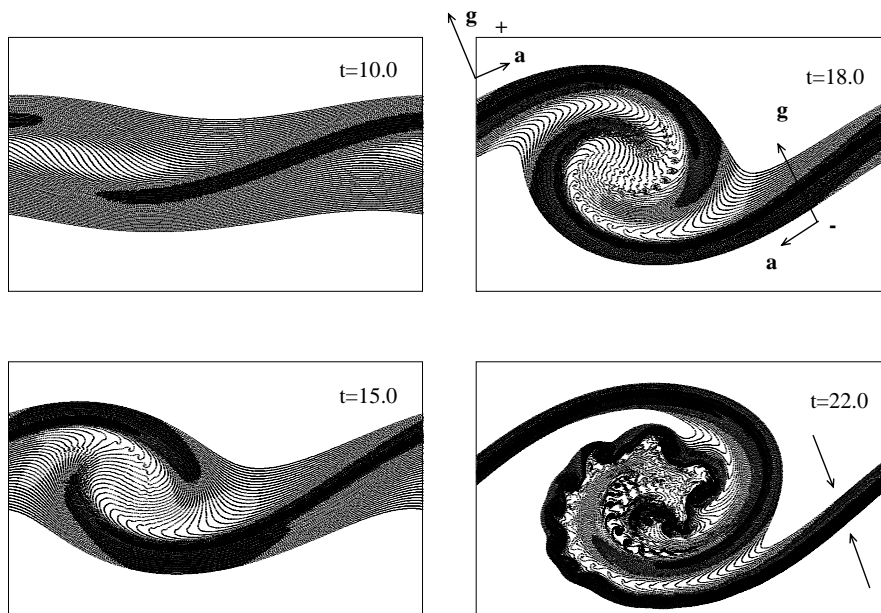


Figure 5: Evolution of the temporal mixing layer mapped with 73 isopycnic lines (with 19272 elements at $t=0$)

the temporal evolution of the layer. The expected development of the primary Kelvin-Helmholtz instability is rapidly established. Then the baroclinic torque intensifies the negative vorticity on the bottom light-side of the structure, while it removes vorticity from the top heavy-side of the vorticity sheet. The braids experience a parallel straining field and baroclinic generation/destruction of vorticity. While the first phenomenon is known to stabilize a vorticity layer [20], the second one enhances the receptivity of the light-side braid by reducing its characteristic time-scale. This is proposed as the basic process that leads to secondary break-ups in the favored light-side braid while the heavy-side one, vorticity deprived, remains stable.

The ability of the calculation to capture these small-scale structures is then investigated by using several time and space steps. The figures 6 and 7 show that the small scale structures are slightly affected by changing the spatial and the temporal resolutions. However, a sequence of secondary structures is clearly identified and reflects a unique response to changing numerically-dependent perturbations. The growth rate of the perturbations, measured from the absolute difference with

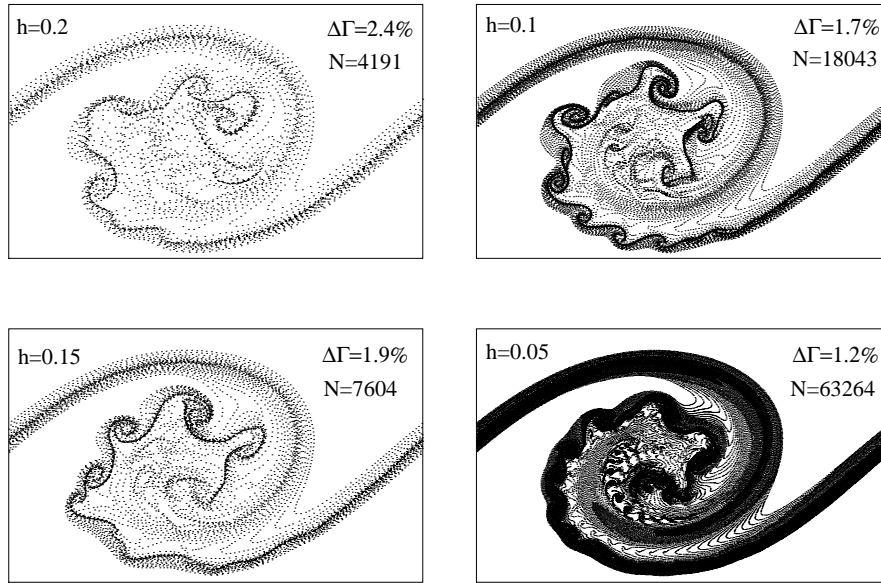


Figure 6: Influence of the spatial resolution at $t = 22.0$ with $dt = 0.1$

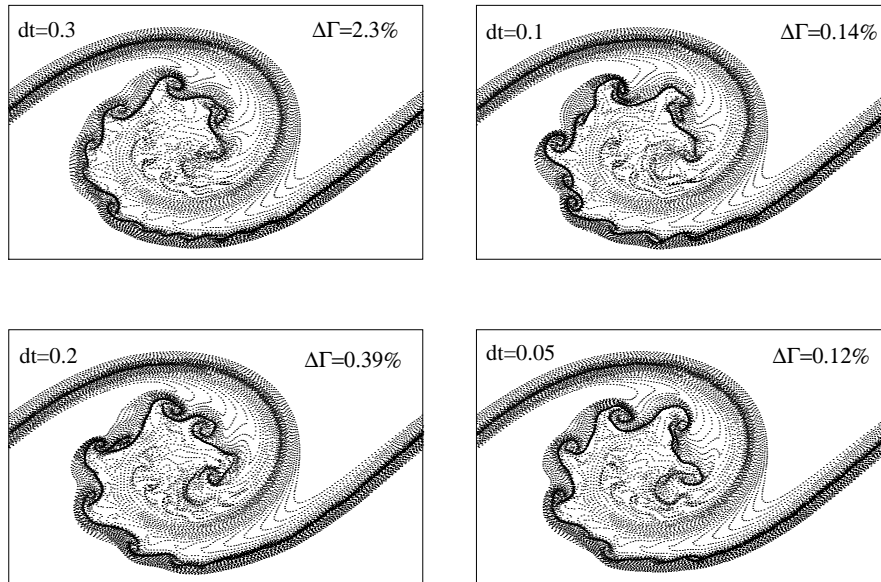


Figure 7: Influence of the temporal resolution at $t = 21.0$ with $h = 0.1$

the unperturbed vorticity layer [8] :

$$\frac{d \ln(I)}{dt} = \frac{d}{dt} \ln \left(\sum_{i=1}^N |\mathbf{u}_i - U(\mathbf{x}_i)| A_i \right) \quad (16)$$

is shown on figure 8 to be insensitive to numerical settings, at least in the present range. After the primary KH structure development, characterized by a standard 0.2 slope, the secondary instability exhibits a slower pace of 0.083, common to all simulations.

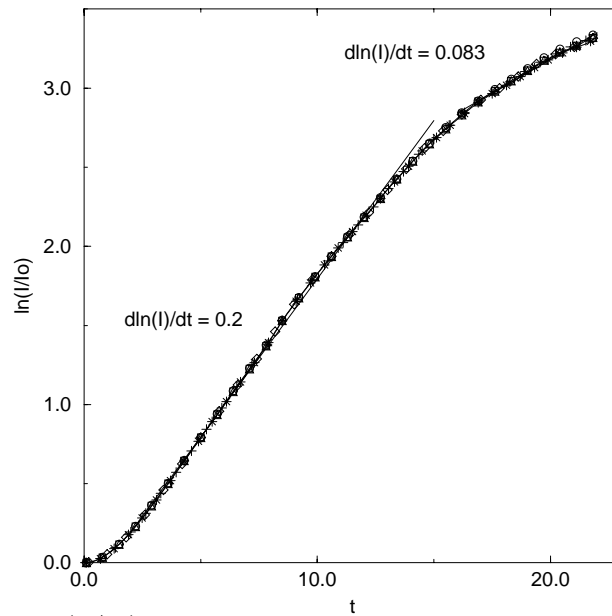


Figure 8: Growth rate: $\ln(I/I_0)$ of the variable-density mixing layer for : $h = 0.2 - dt = 0.1$ (circles), $h = 0.15 - dt = 0.1$ (squares), $h = 0.1 - dt = 0.3$ (solid line), $h = 0.1 - dt = 0.2$ (diamonds), $h = 0.1 - dt = 0.1$ (triangles up), $h = 0.1 - dt = 0.05$ (plus) and $h = 0.05 - dt = 0.1$ (stars)

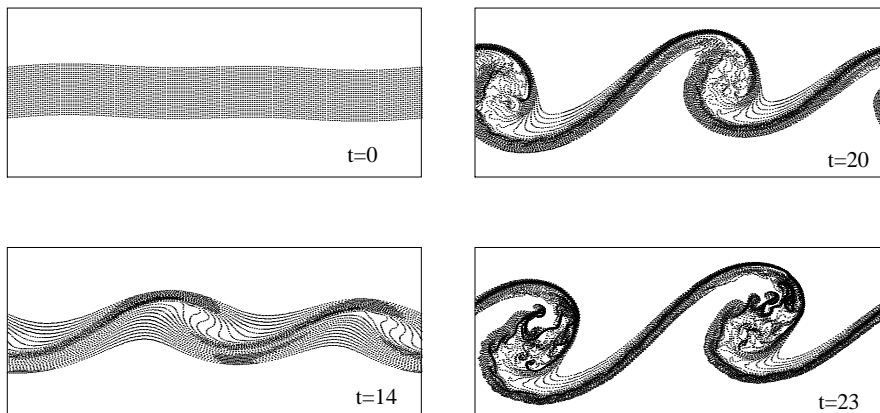


Figure 9: Temporal evolution of the temporal mixing layer with pairing

In the previous calculations, the pairing phenomenon, which naturally appears in a spatially developing layer was neutralized by the boundary conditions. The relevancy of our computations in that respect is now investigated. Thus a temporal layer is perturbed by the most unstable frequency plus its first subharmonic. The amplitude of both perturbations is 1% of the lengthwave $\lambda = 13.2\sigma$. The numerical parameters are: $h = 0.15$, $\delta = 0.18$, $\Delta l_{max} = 0.22$, $\Delta l_{min} = 0.08$, $dt = 0.1$ the density ration is $\rho_1/\rho_2 = 3.0$ and the layer is mapped by 25 isopycnic lines. The figure 9 shows how the secondary instabilities arise before the pairing mode. As in the monochromatic case, the secondary eddies emerge on the low-density side again. The intensification of the negative vorticity braid is strong enough to concentrate vorticity into small-scale structures before the usual large scale pairing is completed.

5 Conclusion

Following Ghoniem *et al* [5,3,4] we study purely inertial effects due to density variations using the so-called transport element method. Some light is shed on the accurate evaluation the baroclinic torque through high order numerical schemes. Highly resolved simulations lead to a proper evaluation of the baroclinic torque for long integration time as it can be tested from the circulation invariance. In a first part we give a simple explanation of the inertial/baroclinic effects by simulating a accelerated stratified layer. Then the development of small-scale, secondary structures in a variable-density temporal mixing-layer is established. The intensification of the negative vorticity in the stretched light-side braid yields a strongly unstable vortex sheet. This secondary mode survives to the forcing of the pairing mode.

References

- 1 LELE S.: CRT Report **N89-22827** (1989).
- 2 STAQUET C.: Two-dimensional secondary instabilities in a strongly stratified shear layer. *J. Fluid Mech.*, **296** (1995), 73–126.
- 3 SOTERIOU M.C., KNIO O.M., AND GHONIEM A.F.: Manipulation of the growth rate of a variable density, spatially developing mixing layer via external modulation. AIAA paper **91-0081** (1991).
- 4 SOTERIOU M.C. AND GHONIEM A.F.: Effects of the free-stream density ratio on free and forced spatially developing shear layers. *Phys. Fluids A*, **7(8)** (1995), 2036.
- 5 GHONIEM A.F., HEIDARINEJAD G., AND KRISHNAN A.: On mixing, baroclinicity and the effect of strain in a chemically-reacting shear layer. AIAA paper **88-0729** (1988).
- 6 ANDERSON C.R.: A vortex method for flows with slight density variations. *J. Comp. Phys.*, **58** (1985), 188–208.
- 7 KRISHNAN A. AND GHONIEM A.F.: Simulation of a rollup and mixing in rayleigh-taylor flow using the transport element method. *J. Comp. Phys.*, **99** (1992), 1.
- 8 GHONIEM A.F., HEIDARINEJAD G., AND KRISHNAN A.: Numerical simulation of a thermally stratified shear layer using the vortex element method. *J. Comp. Phys.*, **79** (1988), 135.
- 9 TURNER J.S.: Buoyancy effects in fluids. Cambridge University Press, Cambridge, (1973).
- 10 MICHALKE A.: *J. Fluid Mech.*, **19** (1964), 543.
- 11 CHORIN A.J.: Numerical study of slightly viscous flow. *J. Fluid Mech.*, **57** (1973), 785.
- 12 BEALE J.T. AND MAJDA A.: High order accurate vortex methods with explicit velocity kernels. *J. Comp. Phys.*, **58** (1985), 188–208.
- 13 PUCKETT E.G.: Vortex methods an introduction and survey of selected research topics. In R. Nicolaides and M. Ginzburger, editors, *Incompressible Computational Fluid Mechanics*. Cambridge University Press, (1992).
- 14 CHORIN A.J.: Vorticity and Turbulence. Number 103 in *Applied mathematical sciences*. Springer, New York, (1994).
- 15 LEONARD A.: Vortex methods for flow simulation. *J. Comp. Phys.*, **37** (1980), 289–335.
- 16 DIMOTAKIS P.: Two-dimensionnal shear-layer entrainment. AIAA journal, **24** (1986), 1791–1796.
- 17 CORCOS G.M. AND SHERMAN F.S.: The mixing layer : deterministic models of a turbulent flow. part 1. introduction and the two-dimensionnal flow. *J. Fluid Mech.*, **139** (1984), 29–65.
- 18 GRINSTEIN F.F., ORAN E.S., AND BORIS J.P.: Numerical simulations of asymmetric mixing in planar shear flows. *J. Fluid Mech.*, **165** (1986), 201–220.
- 19 BROWN G.L. AND ROSHKO A.: On density effects and large structure in turbulent mixing layers. *J. Fluid Mech.*, **64** (1974), 775.
- 20 DRITSCHEL D.G., HAYNES P.H., JUCKES M.N. AND SHEPHERD T.G.: The stability of a two-dimensional vorticity filament under uniform strain. *J. Fluid Mech.*, **230** (1991), 647–665.